Petroleum Science 22 (2025) 5084–5096

Contents lists available at ScienceDirect

Petroleum Science

journal homepage: www.keaipublishing.com/en/journals/petroleum-science

Original Paper

Study on flow capacity and percolation behavior of hydraulically induced bedding fracture by different fluids in full-diameter shale cores

Hong-Tao Fu [a,b], Kao-Ping Song [a], Er-Long Yang [c], Yu Zhao [d], Xi Xia [e], Li-Hao Liang [e,f,*]

[a] Unconventional Petroleum Research Institute, China University of Petroleum (Beijing), Beijing, 102249, China
[b] School of Mechanics and Engineering Science, Peking University, Beijing, 100871, China
[c] School of Petroleum Engineering, Northeast Petroleum University, Daqing, 163318, Heilongjiang, China
[d] Research Institute of Exploration and Development of Daqing Oilfield Company Ltd., Daqing, 163712, Heilongjiang, China
[e] School of Petroleum Engineering, China University of Petroleum (Beijing), Beijing, 102249, China
[f] Research Institute of Petroleum Exploration & Development, Beijing, 100083, China

ARTICLE INFO

Article history:
Received 18 January 2025
Received in revised form
22 September 2025
Accepted 22 September 2025
Available online 25 September 2025

Edited by Jia-Jia Fei

Keywords:
Shale
Fracture extension
Bedding fracture
Flow capacity
Fluid percolation

ABSTRACT

China's continental shale exhibits favorable geological characteristics and substantial resource potential, yet oil recovery for natural energy extraction remains critically low. Investigating the mechanisms of hydraulically induced bedding fracture to generate complex fracture networks in continental shale, and establishing effective flow systems, is of utmost importance. This study employs laboratory experiments and numerical simulations to investigate the flow capacity and percolation behavior of hydraulically induced bedding fractures by different fluids in full-diameter shale cores. Hydraulic stimulation using different fluids generates bedding plane fracture networks, establishing effective flow systems. Eroded and detached shale fragments support localized fractures, thereby increasing their opening and enhancing flow capacity. Cetyltrimethylammonium bromide (CTAB) solution and SiO_2 solution reduce the hydration of the shale surface, preventing shale fragments from swelling and disintegrating, leading to more stable percolation behavior. Eroded and spalled shale fragments near the injection point are transported to farther locations, where they help support localized fractures. This process differs from conventional hydraulic fracturing. Under a constant injection rate, the velocity in the smaller flow paths near the closure is significantly higher than that in the main flow paths, leading to pronounced bypass flow behavior. This restricts the percolation of fluid during imbibition in shale cores. The results provide valuable insights into the mechanism of hydraulically induced bedding fracture in continental shale, offering guidance for the effective development of shale reservoirs.
© 2025 The Authors. Publishing services by Elsevier B.V. on behalf of KeAi Communications Co. Ltd. This is an open access article under the CC BY-NC-ND license (http://creativecommons.org/licenses/by-nc-nd/4.0/).

1. Introduction

In recent years, shale oil has emerged as another hotspot in global unconventional oil and gas exploration and development, following tight oil (Hu et al., 2020; Dou et al., 2022; Gao et al., 2024). Globally, shale oil production, primarily from marine deposits, has been rapidly expanding. The development of shale oil in the United States has played a pioneering role, triggering the global 'shale oil revolution' (Shakya et al., 2022; Kim et al., 2023; Mcmahon et al., 2024). Unlike the marine deposits in the United States, China's shale oil resources are primarily from continental deposits. Preliminary estimates suggest that the geological resource of mature shale oil in continental deposits is approximately 200×10^8 t, with technically recoverable reserves reaching 43.9×10^8 t, about 54.7% of the technically recoverable reserves of conventional oil and gas (Zhou et al., 2023; EIA, 2013). These resources are primarily distributed in basins such as Songliao, Ordos, and Junggar (Yang et al., 2021; Wang et al., 2022a, 2022b; Zhao et al., 2024). With China's growing energy demand, efficient development of shale oil reservoirs has become one of the

* Corresponding author.
E-mail address: Petrolihao@163.com (L.-H. Liang).
Peer review under the responsibility of China University of Petroleum (Beijing).

https://doi.org/10.1016/j.petsci.2025.09.035
1995-8226/© 2025 The Authors. Publishing services by Elsevier B.V. on behalf of KeAi Communications Co. Ltd. This is an open access article under the CC BY-NC-ND license (http://creativecommons.org/licenses/by-nc-nd/4.0/).

effective solutions to address its current energy shortage. The Chinese government is accelerating the efficient development of continental shale oil to ensure its energy security.

The Gulong shale oil, located in China's Songliao Basin, a typical representative of continental shale oil, has an estimated geological reserve of 12.7×10^8 t (Sun et al., 2023; Wang et al., 2023a, 2023b). It is characterized by a complex mineral composition, poor physical properties, and well-developed bedding fractures (He et al., 2023; Sun et al., 2023; Wang et al., 2023a, 2023b; Meng et al., 2024). As it is a novel resource type, no geological theories or development technologies derived from global experience can be directly applied, making the development process particularly challenging (Sun et al., 2021, 2023; Song et al., 2024). After the implementation of multi-stage horizontal well fracturing technology in the continental shale of Songliao Basin, natural energy rapidly declined, resulting in a low oil recovery of around 5%. Previous studies have shown that the application of imbibition by injected fluids significantly improves the recovery of shale oil reservoirs (Zhang et al., 2023a, 2023b; Guo et al., 2024). However, in continental shales with high clay content and well-developed bedding fractures, new hydraulic fractures are formed during the imbibition process (Lv and Hou, 2024; Zhao et al., 2024; Fu et al., 2024). The shale oil flow system created by hydraulic induction through injected fluids plays a key role in the efficient development of continental shale oil.

In recent years, the mechanism of hydraulically induced fracturing in continental shale by injected fluids has become a research hotspot. Studies have shown that the clay mineral content is a major factor influencing permeability damage due to hydration of shale. Significant damage occurs when the clay mineral content in shale exceeds 15% (Zhang et al., 2017). In shale with bedding fractures, the bedding planes restrict the height of hydraulically induced fracture propagation, with the fracture tips remaining within the bedding planes (Zhang et al., 2024a). He et al. (2020) further proposed that hydraulically induced micro-fractures primarily propagate along the mineral-organic matter interfaces. Zhuang et al. (2014) found that significant dissolution occurred during the water-shale interaction, promoting the formation of new fractures. The dissolution of shale is primarily caused by carbonate minerals, such as calcite. Ma et al. (2016) suggested that shale hydration fundamentally depends on the clay mineral content and free water invasion. Water invasion is influenced by capillary effects, intrusion along bedding planes and micro-fractures, pore pressure propagation, chemical reactions, and other processes. In these studies, the injected fluids were either pure water or formation water. In contrast, China's continental shale oil reservoirs are oil-wet or mixed-wet (Wang et al., 2022a, 2022b). To achieve spontaneous imbibition and enhance oil recovery, surfactant solutions or nanofluids must be used to modify the wettability of shale surfaces (Liu et al., 2019; Hou and Sheng, 2022). Therefore, it is crucial to investigate the mechanisms by which different injected fluids activate bedding fractures and establish effective flow systems in continental shale. In addition, clarifying the associated flow capacity and percolation behavior is essential for improving production stability and maximizing recovery in continental shale oil reservoirs.

In this study, full-diameter shale cores from the Songliao Basin were used to conduct experiments on hydraulic fracture propagation induced by different fluids, aiming to evaluate the flow capacity of the resulting fractures. Based on the experimental results, numerical simulations were conducted to investigate the percolation behavior of different fluids within the hydraulically induced fractures.

2. Geological overview of coring well

The Songliao Basin, located in northeastern China, trends northeast with a length of approximately 750 km and a width ranging from 330 to 370 km. It is a typical continental rift-depression lake basin and is considered one of the most resource-rich oil and gas basins in the world (Fig. 1(a)) (Li et al., 2024; Yu et al., 2024; Xiao et al., 2024). The experimental cores were collected from the Qijia-Gulong Sag (Fig. 1(b)).

The Songliao Basin developed mainly during the Cretaceous, with large-scale lake transgressions occurring in the Late Cretaceous, particularly during the deposition of the Qingshankou and Nenjiang formations, leading to the widespread distribution of semi-deep to deep lacustrine deposits. In the Qingshankou Formation, a major lake transgression formed a large and stable lake basin (Li et al., 2024; Yu et al., 2024; Xiao et al., 2024). Based on lithological and compositional characteristics, the main productive intervals of the shale formation (Q1 and lower Q2 members) are

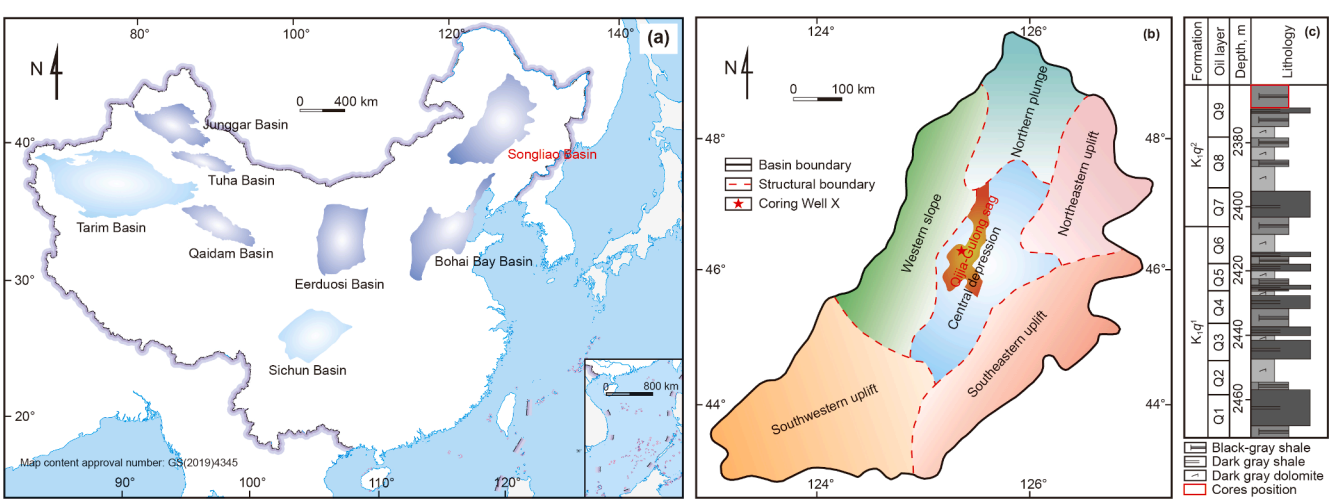

Fig. 1. Location and lithology of coring Well X in the Songliao Basin: (**a**) Songliao Basin in northeastern China; (**b**) location of coring Well X in the Qijia-Gulong Sag; (**c**) lithology of the Qingshankou Formation in coring Well X (modified from Zhao et al., 2023).

subdivided into nine oil layers, with a total thickness of 80–130 m (Fig. 1(c)) (Zhou et al., 2023). Full-diameter cores were obtained from the Q9 layer, which is classified as pure shale-type shale. These cores exhibit well-developed bedding fractures, with relatively straight fracture surfaces and a fracture density of 500–1000 bedding fractures per meter.

3. Methodology

3.1. Experimental materials and methods

3.1.1. Materials

The experimental materials included full-diameter shale cores from coring Well X of the Qingshankou Formation in the Songliao Basin (diameter × length = 11 × 12 cm); silicone mold (length × width × height = 10 × 10 × 10 cm); deionized water; KCl (Shanghai Aladdin Biochemical Science and Technology Co., Ltd., purity≥ 99.98%); CTAB (Shanghai Aladdin Biochemical Science and Technology Co., Ltd., purity≥ 99.0%); SiO_2 nanofluid stock solution (prepared by the China University of Petroleum (East China), average particle size = 6 nm); epoxy resin adhesive (AB crystal adhesive, mixed at a 3:1 ratio); acrylic structural AB adhesive (Germany Kisling Company, mixed at a 1:1 ratio); steel pipe (outer diameter = 8 mm, inner diameter = 6 mm).

3.1.2. Methods

(1) **Core sample preparation**

① The full-diameter cores (Fig. 2(d)) were cut into cubic shale cores with dimensions of 9 cm × 9 cm × 9 cm using a wire-cutting apparatus, and each was placed into a silicone mold. Cylindrical shale cores (diameter × length = 2.5 × 4 cm) were machined from the remaining shale material, with horizontal air permeability and porosity subsequently measured through laboratory tests.

② The cubic shale core was placed at the center of a 10 cm × 10 cm × 10 cm silicone mold. Epoxy resin adhesive was then poured into the mold and cured for 24 h (Fig. 2(f)). To prevent deformation of the mold, acrylic plates were used to secure it. The encapsulated core was designed to fit into a 10 cm × 10 cm × 10 cm core holder. Additionally, the epoxy resin layer prevented mechanical damage to the sample during subsequent drilling and pressure release.

③ The encapsulated shale core was removed, and a 4.5 cm deep circular hole was drilled along the vertical bedding direction using an 8 mm drill bit.

④ A 6 cm long steel pipe was inserted into the hole and fixed using acrylic structural AB resin, then cured for 24 h.

⑤ A 6 mm diameter drill bit was used to drill a 5.5 cm deep hole, from the upper surface of the core, completing the core preparation after encapsulation and tube insertion (Fig. 2(e)).

(2) **Hydraulically induced fracture expansion experiment**

① The cubic shale cores were scanned and reconstructed using an X-ray CT scanner before the steel pipe was fixed following drilling. The resolution of the CT scan was 53 μm.

② A 0.75% (mass fraction) KCl solution was prepared, using the KCl solution as the base fluid, a 0.1% CTAB solution, a 0.1% SiO_2 solution, and a 0.1% mixed solution of CTAB and SiO_2 (CTAB: SiO_2 nanofluid = 1:1) were prepared.

③ The prepared fluid was introduced into the intermediate container, the outlet end was closed, and the device was checked for leakage.

④ The core, after encapsulation and tube insertion, was placed in the core chamber of the true triaxial fracturing experimental apparatus, and a constant pressure of 8 MPa was applied in the *x*, *y*, and *z* directions.

⑤ The fluid was injected into the shale core at a flow rate of 10 mL/min until the peak pressure was reached.

⑥ The fluid was injected at flow rates of 0.5, 1, 2, 3, 4, 5, and 6 mL/min, with the flow rate adjusted every 2 min, and the injection pressure was recorded.

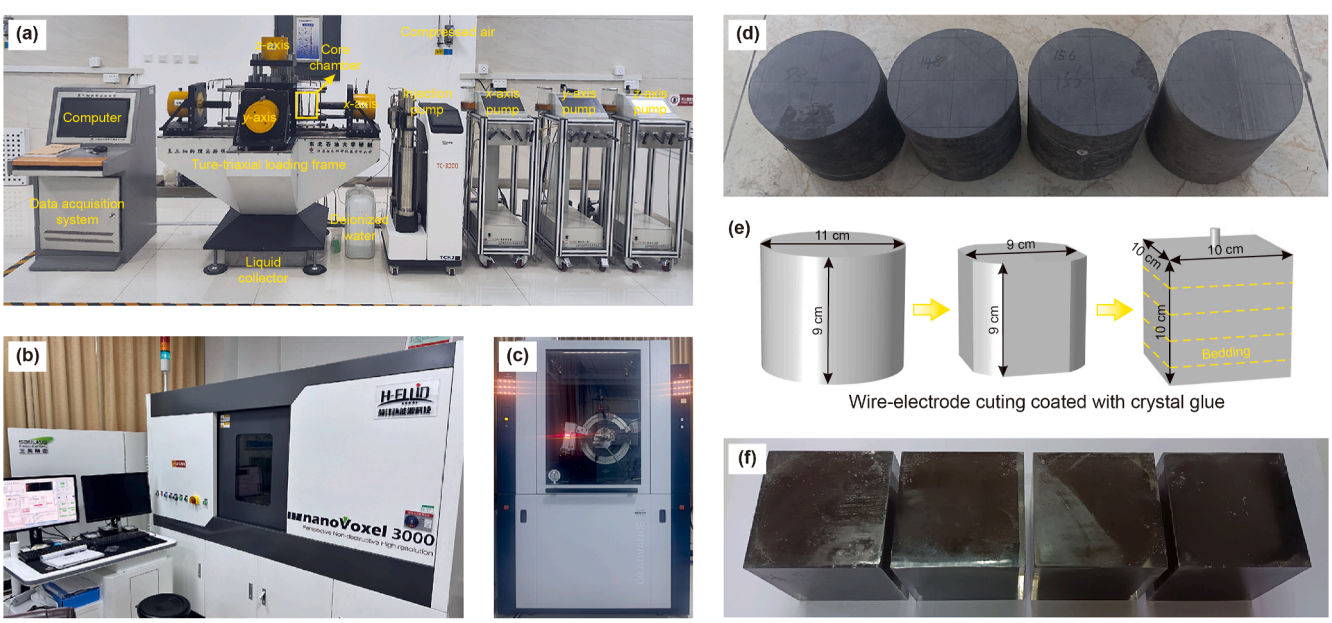

Fig. 2. Experimental equipment and prepared cores: (**a**) true triaxial hydraulic fracturing experimental system; (**b**) nanoVoxel 3000 X-ray CT scanner (resolution: 0.5 μm); (**c**) D8AA25 high-resolution X-ray diffractometer (Bruker, Germany); (**d**) full-diameter cores from coring Well X; (**e**) core preparation process for hydraulic fracturing; (**f**) cubic shale cores coated with epoxy resin adhesive.

⑦ The steel pipe inside the core was removed, and the core was scanned and reconstructed using an X-ray CT scanner again. AVIZO software was used for fracture extraction (Avizo, 2019). CT scanning was performed in accordance with *Microbeam Analysis—Computer Tomography (CT) Imaging Method for Micro-Nanopore Structure of Tight Rocks* (GB/T 38531-2020).

3.2. Numerical simulation

3.2.1. Simulation method

(1) **Governing equations**

For viscous fluids, the velocity (u), pressure (p), and density (ρ) at any point in space satisfy the continuity equation based on mass conservation:

$$\frac{\partial \rho}{\partial t} + \nabla \cdot (\rho u) = 0 \tag{1}$$

where

$$\nabla \cdot (\rho u) = \frac{\partial \rho u_x}{\partial x} + \frac{\partial \rho u_y}{\partial y} + \frac{\partial \rho u_z}{\partial z} \tag{2}$$

For incompressible fluids, the density remains constant over time and space. Therefore, the continuity equation simplifies to:

$$\nabla \cdot u = 0 \tag{3}$$

Let the body force per unit volume be F and the surface stress per unit volume be $\nabla \cdot \sigma$. According to Newton's second law:

$$\rho \frac{Du}{Dt} = \rho F + \nabla \cdot \sigma \tag{4}$$

where σ is the total stress.

$$\sigma = -p\boldsymbol{I} + \tau \tag{5}$$

$\frac{Du}{Dt}$ is the particle acceleration:

$$\frac{Du}{Dt} = \frac{\partial}{\partial t} u + (u \cdot \nabla) u \tag{6}$$

For elastic solids, the relationship between deformation and stress follows Hooke's law, while for viscous fluids, it follows Stokes' law.

$$\tau = \mu \left(\nabla u + \nabla u^{\mathrm{T}} \right) \tag{7}$$

Based on the derivation of the continuity equation and Newton's second law, the Navier-Stokes equation for incompressible fluids can be obtained under the assumption of negligible gravity. The steady-state flow within the fractures is solved by using the Navier-Stokes equations (Panton, 2013).

$$\begin{cases} \rho \left[\frac{\partial u}{\partial t} + (u \cdot \nabla) u \right] = \nabla \left(-p\boldsymbol{I} + \mu [\nabla u + (\nabla u)^{\mathrm{T}}] \right) \\ \nabla u = 0 \end{cases} \tag{8}$$

where ρ is fluid density, kg/m^3; u is fluid velocity, m/s; t is time, s; p is fluid pressure, Pa; $\boldsymbol{I}$ is identity matrix; μ is fluid viscosity, Pa·s.

(2) **Boundary conditions**

The boundary conditions for each model are as follows: the left side is the inlet and the right side is the outlet, with specified velocities at the inlet. The outlet pressure is set to 0, and the shale surface is treated as a no-slip boundary.

Inlet boundary condition:

$$u = u_0, \boldsymbol{n} \cdot \mu \left(\nabla u + (\nabla u)^{\mathrm{T}} \right) = 0 \tag{9}$$

Outlet boundary condition:

$$p = p_0, \boldsymbol{n} \cdot \mu \left(\nabla u + (\nabla u)^{\mathrm{T}} \right) = 0 \tag{10}$$

Solid wall boundary:

$$u = 0 \tag{11}$$

where $\boldsymbol{n}$ is the unit normal vector.

3.2.2. Model design and assumption

(1) **Model design**

In the simulation process, the viscosity of the injected fluid was 1 mPa·s, and its density was 1000 kg/m^3. The injection velocity was 0.1 m/s, and the outlet pressure was 0 Pa The hydraulically induced fractures of different fluids in the experiment were extracted using Avizo software (Avizo, 2019). For the numerical simulations, representative localized fractures corresponding to each fluid were selected, with dimensions of 5.3 mm (length) × 3.7 mm (width). The boundary layer thickness and mesh size of the partial fractures in each core were set to 5 μm. The total number of grids for each simulation case is listed in Table 1.

(2) **Model assumptions**

This study employs a laminar flow model (Stokes flow) to simulate the percolation behavior of different fluids in microfractures within porous media. To simplify the computations, the following assumptions are made:

① The injected fluid is considered incompressible.
② The fluid is assumed to remain isothermal throughout the percolation process.
③ All fluids are assumed to have identical density and viscosity.
④ Gravitational effects are neglected due to the small scale of the model.

4. Results and discussion

4.1. Mineral composition and physical characteristics of shale cores

The mineral composition of shale influences its mineralization reactions and mechanical properties (Zhao et al., 2023; Zhou et al., 2023; Hong et al., 2024). To characterize the physicochemical properties of the full-diameter shale samples used in this study, X-ray diffraction was employed to analyze the mineral composition of the core samples. The results are presented in Fig. 3(a) for overall mineral composition and Fig. 3(b) for clay mineral

Table 1
Mesh division for partial fractures in different shale cores.

Core number	S156	S148	S93	S132
Fluid types	KCl solution	CTAB solution	SiO_2 solution	CTAB and SiO_2 mixed solution
Number of grids	2404557	3625455	2730596	2077997

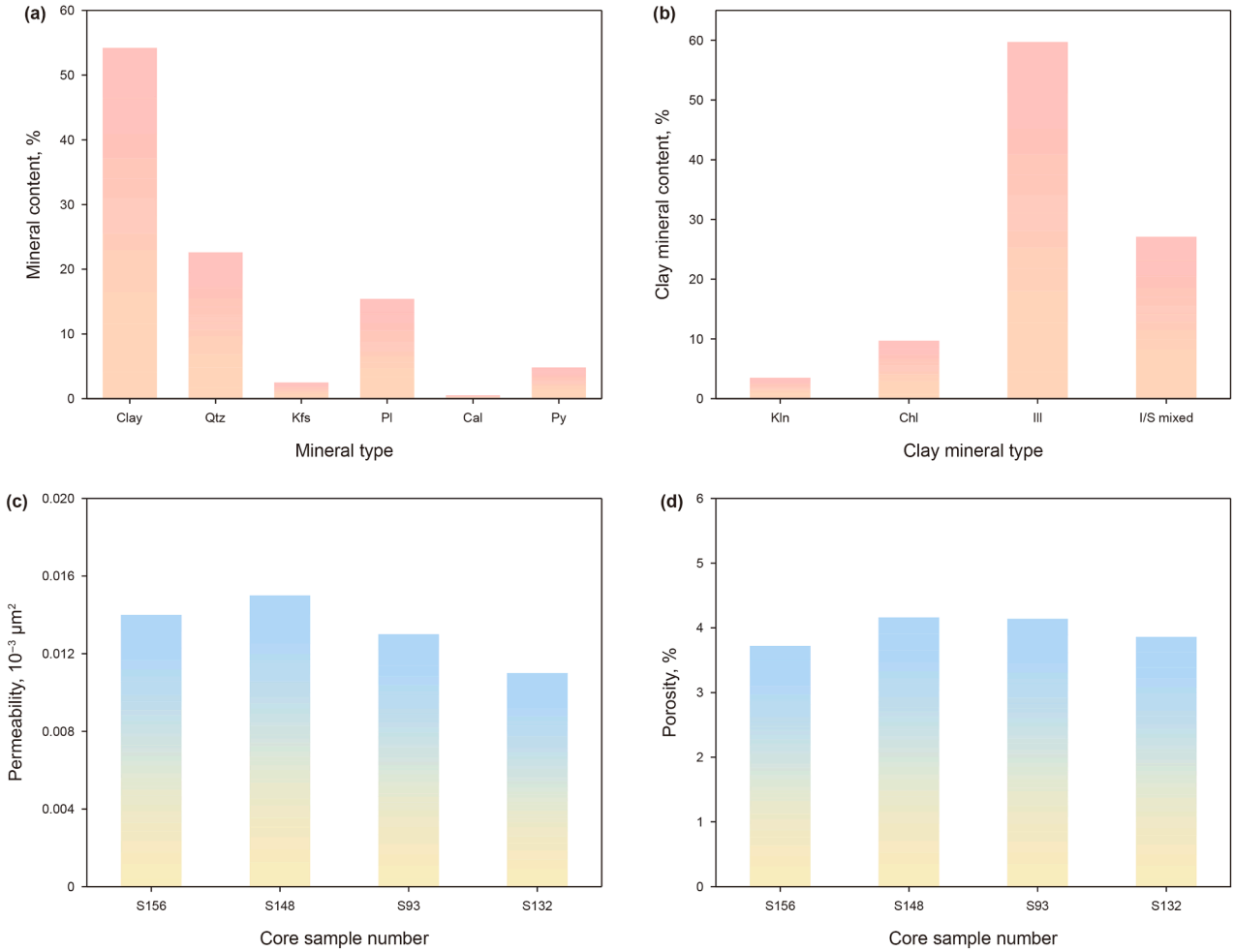

Fig. 3. Mineral composition and porosity-permeability characteristics: (**a**) mineral content of core S148; (**b**) clay mineral content of S148; (**c**) permeability of different full-diameter cores; (**d**) porosity of different full-diameter cores.

composition. The shale primarily consists of clay minerals, quartz, and plagioclase, with clay accounting for 54.2%, quartz 22.6%, and plagioclase 15.4%. Compared to shale oil reservoirs in other basins, the clay mineral and plagioclase contents are relatively higher (Zhou et al., 2023). The clay mineral composition is dominated by illite, illite-montmorillonite mixed-layer, and chlorite. The illite content is 59.7%, illite-montmorillonite mixed-layer content is 27.1%, and chlorite content is 9.7%. The shale in the Songliao Basin has undergone advanced diagenesis, resulting in the transformation of montmorillonite into illite and the concurrent precipitation of silica, thereby enhancing the rigidity and brittleness of the shale (Sun et al., 2021).

The porosity of the full-diameter shale cores ranges from 3.7% to 4.2%, with an average of 4.0% (Fig. 3(c)). The horizontal permeability varies from 0.011×10^{-3} to 0.015×10^{-3} μm^2, with an average of 0.013×10^{-3} μm^2 (Fig. 3(d)). These porosity and permeability values indicate poor reservoir quality. Macroscopic observations reveal numerous bedding fractures on the shale surface, which may facilitate fluid invasion along these natural fractures (Sun et al., 2023; Shi et al., 2023).

4.2. Experiment on hydraulically induced fractures

The variation characteristics of injection pressure curves are essential for understanding hydraulic fracture propagation in shale (Yang et al., 2022, 2023; Li et al., 2023). The time-pressure curves of hydraulically induced fractures in full-diameter shale cores with different fluids are shown in Fig. 4. When injecting KCl solution, the injection pressure reached 61.1 MPa, inducing hydraulic fracturing along the bedding planes, followed by a sharp drop to 12.9 MPa (Fig. 4(a)). For the CTAB solution, the injection pressure reached 43.9 MPa, inducing hydraulic fracturing along the bedding planes, and then the injection pressure rapidly decreased to 4.5 MPa (Fig. 4(b)). When injecting the SiO_2 solution, the injection pressure reached 30.5 MPa, inducing hydraulic fracturing along the bedding planes, followed by a rapid drop to 3.3 MPa (Fig. 4(c)). When injecting the CTAB and SiO_2 mixed solution, the injection pressure reached 57.3 MPa, inducing hydraulic fracturing along the bedding planes, and subsequently decreased sharply to 11.1 MPa (Fig. 4(d)). Generally, when the injection pressure is below the breakdown pressure, the fluid fills the wellbore and undergoes wellbore storage and compression, leading to a gradual pressure increase. Once the fracture initiation pressure of the bedding is reached, the weakly cemented shale bedding planes are activated. The fluids then rapidly break through from the wellbore along the induced fractures toward the core edges and flow out, resulting in a sharp drop in injection pressure. It is noteworthy that significant differences exist in the peak pressures required to initiate fractures in full-diameter shale cores through hydration induced by different fluids. These differences can be attributed to variations in the

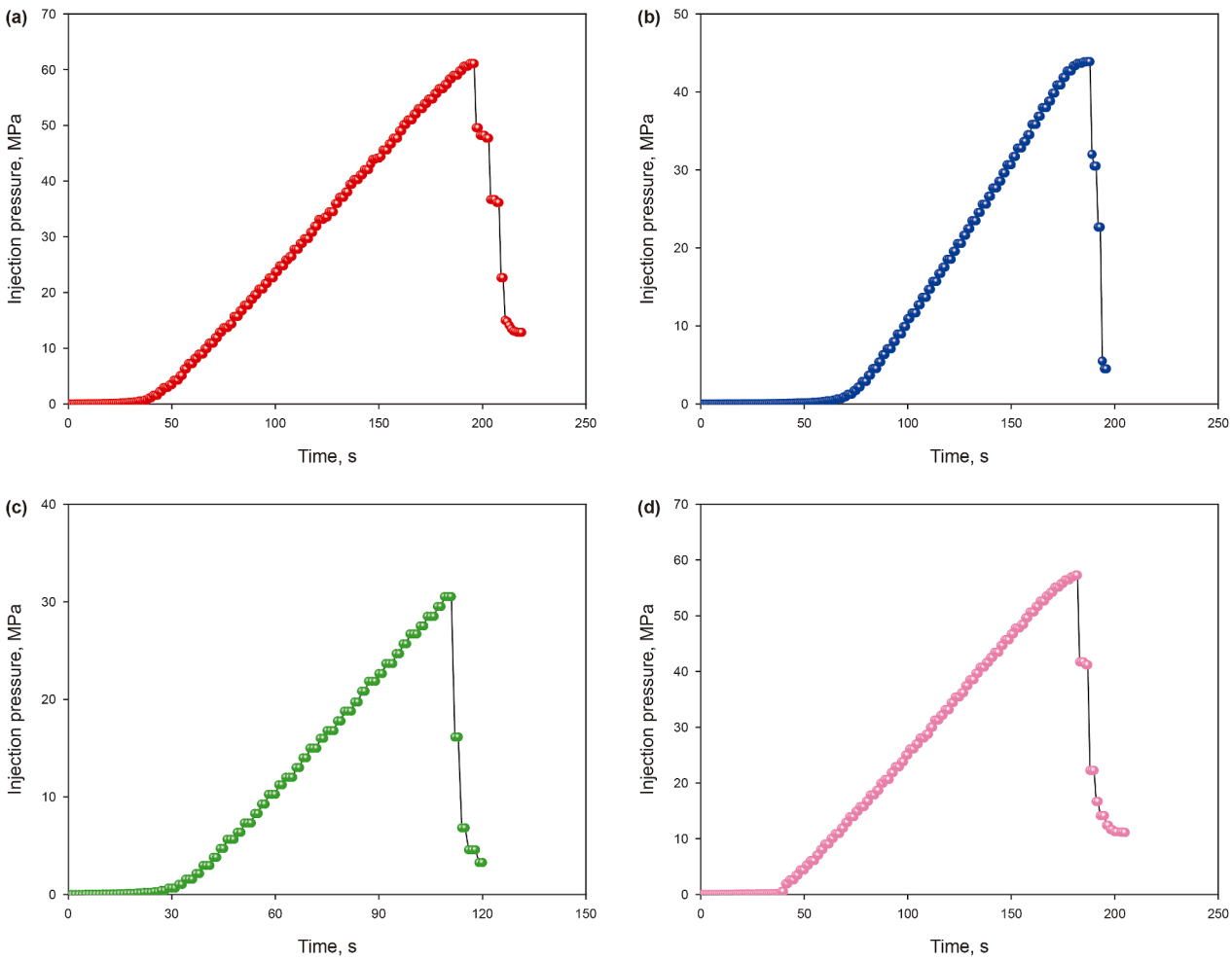

Fig. 4. Injection pressure-time relationships with different fluids: (**a**) core S156 injected with KCl solution; (**b**) core S148 injected with CTAB solution; (**c**) core S93 injected with SiO_2 solution; (**d**) core S132 injected with CTAB and SiO_2 mixed solution.

degree of hydration caused by the different fluids, and pre-existing damage of the internal bedding fractures. Additionally, after hydraulic fracture propagation in full-diameter shale cores with CTAB solution and SiO_2 solution, the injection pressure was influenced by the applied triaxial compressive stress and was lower than the triaxial stress. This suggests that internal fragmentation occurred within the core, with shale fragments supporting the fracture walls and preventing the closure of new induced fractures, thereby enhancing the core's flow capacity.

After hydraulic fractures were induced in full-diameter shale cores by injecting different fluids, each fluid was subsequently injected at increasing rates. The injection rate was incremented every 2 min, and the pressure-time relationship for each fluid was recorded at 1 s intervals (Fig. 5). The hydraulic fractures induced during the experiment propagated through the full-diameter cores and extended to the core surfaces, where the fluid pressure at the fracture tips was atmospheric. A constant triaxial stress of 8 MPa was applied to the full-diameter core. The injection pressure reflects the flow capacity of the induced fractures within the shale core. During the KCl solution injection, when the injection rate was increased to 5 mL/min, the injection pressure initially rose. However, significant pressure declines were observed at both 3 and 5 mL/min injection rates (Fig. 5(a)). When the injection rate reached 6 mL/min, a sharp drop in injection pressure occurred. This indicates that during KCl solution injection, the hydration and erosion effects caused the detachment and migration of larger laminated shale fragments within the preferential flow paths of the core fractures. These shale fragments supported the preferential flow paths within the opened fractures and enhanced their flow capacity. When injecting CTAB solution, increasing the injection rate to 6 mL/min, resulted in a rise in injection pressure across all tested rates, while maintaining relatively stable flow capacity (Fig. 5(b)). This indicates that the hydraulically induced fractures created by CTAB solution injection possess stable internal structures, where eroded, spalled, and transported shale fragments support the localized open fractures, leading to more stable flow capacity. When injecting the SiO_2 solution, increasing the injection rate to 6 mL/min resulted in fracture flow capacity that was relatively stable and similar to that observed with CTAB solution injection (Fig. 5(c)). This suggests that both the CTAB solution and SiO_2 solution further suppressed shale surface hydration compared to the KCl solution, leading to more stable mechanical properties at the fracture contact surfaces. Some studies have shown that hydration can significantly destabilize the surface stability and mechanical properties of shale (Cui et al., 2023; Hong et al., 2024). However, both CTAB and SiO_2 can promote the contraction of clay interlayer spacing, enhance the stability of clay mineral crystals, and maintain their mechanical performance,

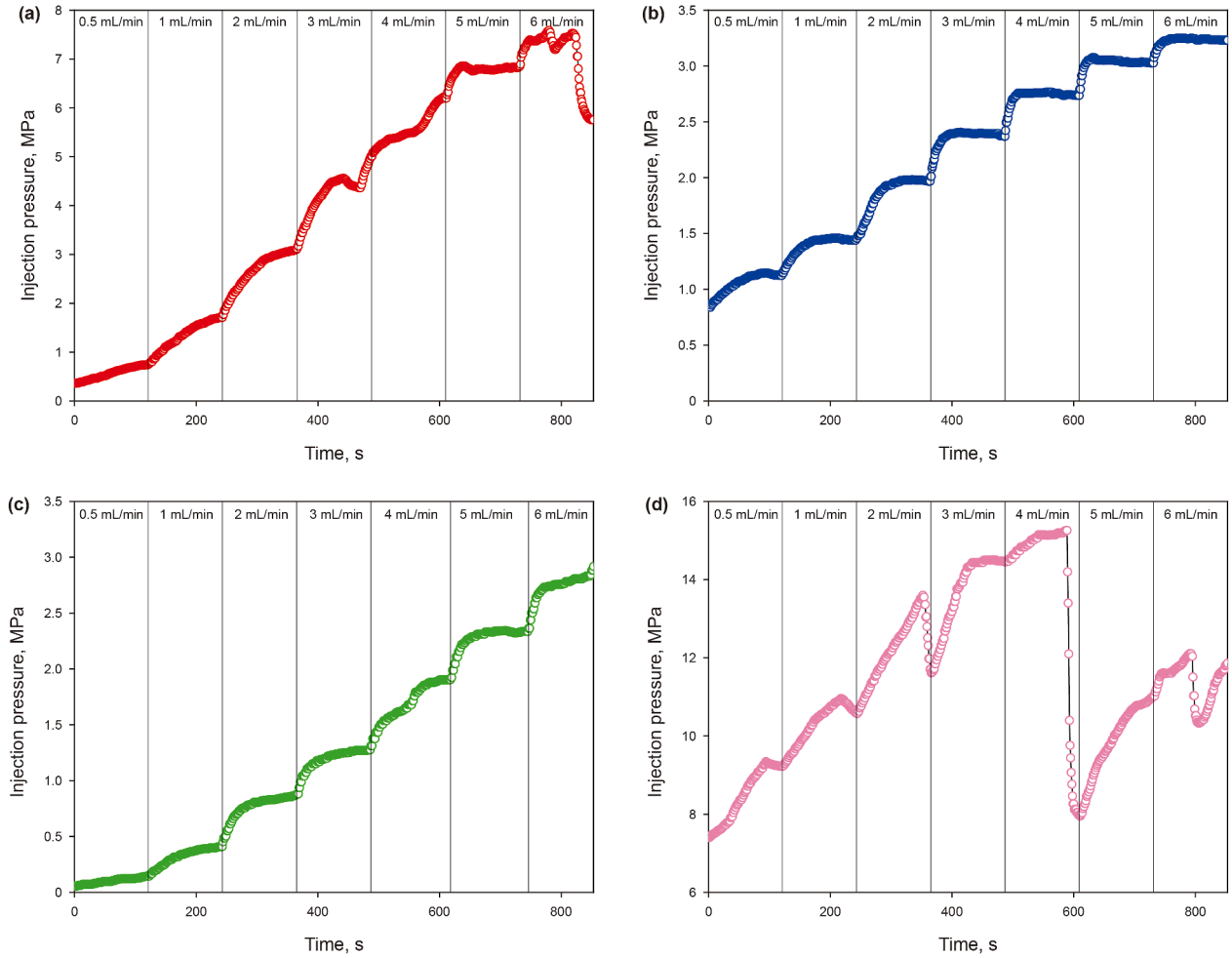

Fig. 5. Injection pressure-time relationships for different fluids after fracture initiation in full-diameter cores: (**a**) core S156 with KCl solution; (**b**) core S148 with CTAB solution; (**c**) core S93 with SiO_2 solution; (**d**) core S132 with CTAB and SiO_2 mixed solution.

thereby inhibiting the transport of water molecules within the clay minerals (Shi et al., 2023; Karimi et al., 2023). When injecting the CTAB and SiO_2 mixed solution, increasing the injection rate to 2 and 4 mL/min resulted in a significant pressure drop in the later stages (Fig. 5(d)). However, at injection rates of 3 and 5 mL/min, the injection pressure continued to rise. When the injection rate reached 6 mL/min, the pressure exhibited an initial decline followed by an increase as the injection volume increased. This indicates that during the injection of CTAB and SiO_2 mixed solution, the fluid continuously eroded and transported small detached particles of clay or quartz within the shale core. These mobilized particles subsequently migrated into the flow paths, where they accumulated and eventually blocked the paths.

When the injection pressure within the flow path gradually increases to a certain threshold, the blocked path is flushed open. This results in a process of increasing and then decreasing flow capacity within the core. Therefore, the strong coupling effect between CTAB and SiO_2 in the solution overly suppresses the hydration of shale, which affects the detachment of shale fragments. As a result, the opened fractures are difficult to support effectively and are more prone to closure. A comprehensive comparison of the final flow capacities within hydraulically induced fractures for different fluids reveals the following order: SiO_2 solution (S93) > CTAB solution (S148) > KCl solution (S156) > CTAB and SiO_2 mixed solution (S132).

To investigate the actual fracture propagation induced by different fluids, CT scanning was performed to compare the pre- and post-fracture states of full-diameter shale cores subjected to hydraulic fracture propagation. The reconstructed surface states of the shale cores are shown in Fig. 6. From the reconstructed images of the cores, it was observed that after the KCl solution was injected, a single distinct fracture was formed at the front position of the core. This phenomenon was observed by comparing region I (Fig. 6(a)) to region II (Fig. 6(b)). In contrast, after the CTAB solution was injected, three clear fractures were formed at the front position of the core. This was observed by comparing region III (Fig. 6(c)) to region V (Fig. 6(d)) and region IV (Fig. 6(c)) to region VI (Fig. 6(d)). No significant fractures were observed at the front position of the core after the SiO_2 solution and the CTAB and SiO_2 mixed solution were injected. This indicates that the full-diameter shale cores exhibit significant heterogeneity in the bedding direction, with no obvious pattern in the position of fluid penetration across the core. However, it is notable that the fractures induced by KCl solution and CTAB solution are parallel to the bedding planes.

To further investigate the morphology of hydraulic fractures induced by different fluids, a brightness segmentation method was employed to extract the fracture networks (Zhang et al., 2024b). The resulting fracture distributions in shale cores induced by various fluids are presented in Fig. 7. It was found that hydraulic fractures induced by KCl solution, SiO_2 solution, and CTAB and SiO_2

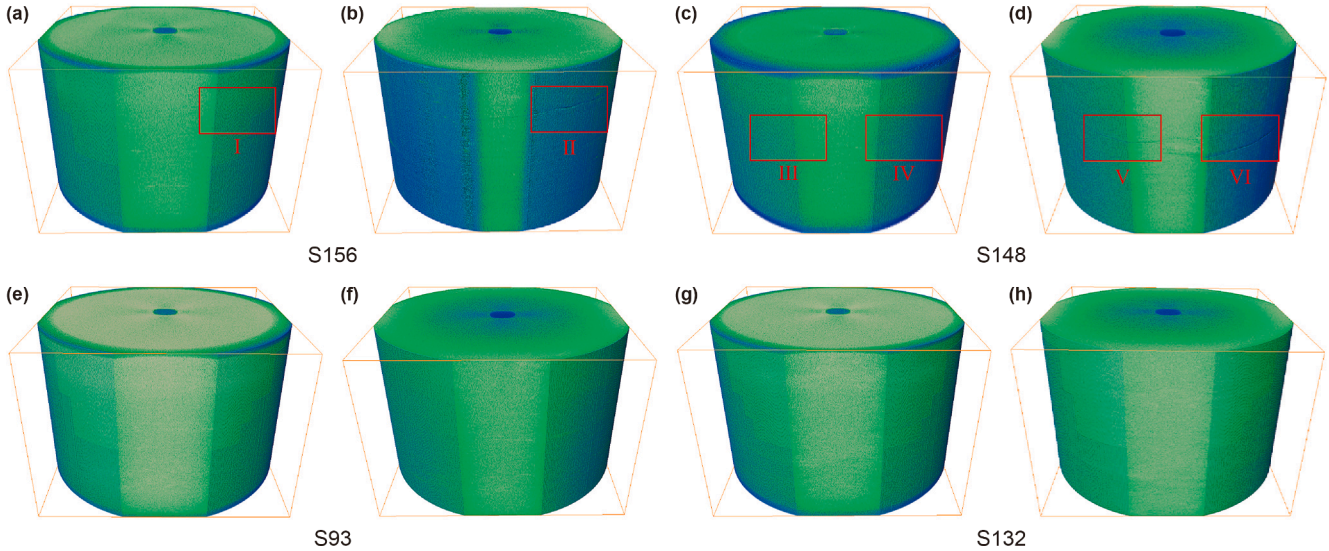

Fig. 6. 3D reconstructed images of hydraulically induced fractures by different fluids in full-diameter cores: (**a**) core S156 before KCl solution injection; (**b**) core S156 after KCl solution injection; (**c**) core S148 before CTAB solution injection; (**d**) core S148 after CTAB solution injection; (**e**) core S93 before SiO_2 solution injection; (**f**) core S93 after SiO_2 solution injection; (**g**) core S132 before CTAB and SiO_2 mixed solution injection; (**h**) core S132 after CTAB and SiO_2 mixed solution injection.

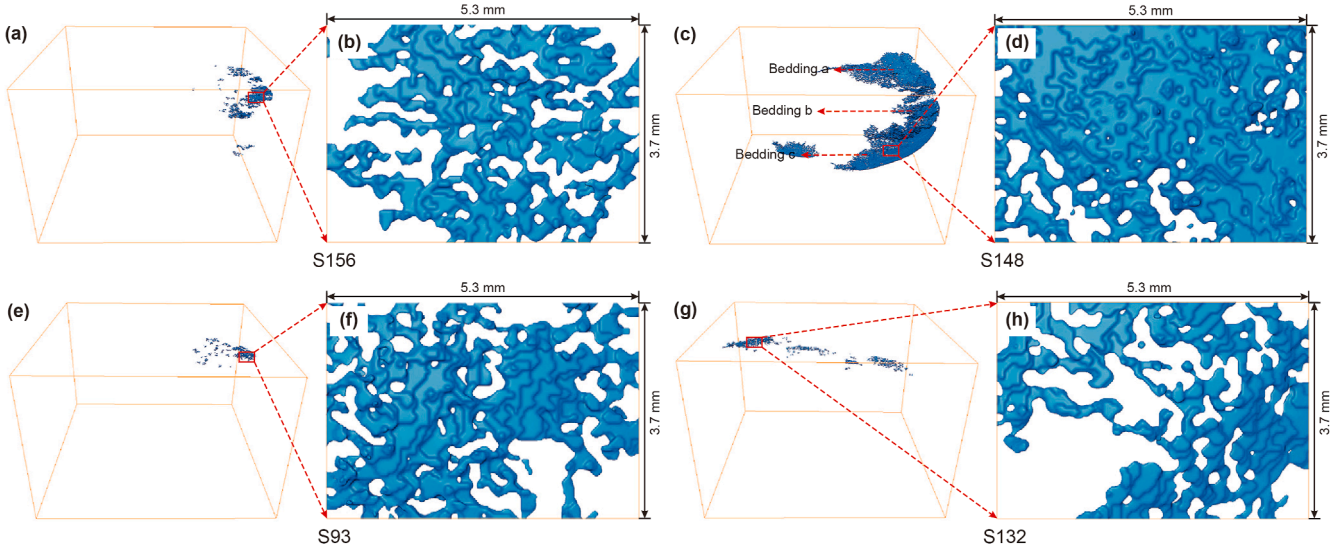

Fig. 7. Hydraulically induced fractures after injection of different fluids: (**a**) core S156 after KCl solution injection; (**b**) partial enlargement of (a); (**c**) core S148 after CTAB solution injection; (**d**) partial enlargement of (c); (**e**) core S93 after SiO_2 solution injection; (**f**) partial enlargement of (e); (**g**) core S132 after CTAB and SiO_2 mixed solution injection; (**h**) partial enlargement of (g).

mixed solution propagated only along a single bedding direction (Fig. 7(a–e), and (g)). The resulting fractures were relatively smooth with no significant change in fracture trajectory. In contrast, hydraulic fractures induced by CTAB solution formed three distinct fractures at different horizontal levels along the bedding planes (Fig. 7(c)). The induced fractures extended only in one direction, with no observed activation on the opposite side. As the distance from the injection point increased, the fracture aperture grew. This further suggests that eroded shale fragments or small particles near the injection point were transported to greater distances, supporting the localized fractures. The aperture of these fractures increased, thereby enhancing their flow capacity. This phenomenon was clearly visible in the magnified images of localized fractures induced by each fluid. These fractures represent localized connectivity, forming complex flow regions. However, the flow patterns within these regions are irregular, and the flow behavior at different locations along the fractures remains difficult to predict.

After hydraulic fracturing of full-diameter cores with different fluids, observations of the upper and lower fracture surfaces revealed the presence of laminated shale fragments at localized positions. These shale fragments were observed at regions I–V (Fig. 8(a–e)). These shale fragments constitute a self-supporting flow system within the shale cores. It was found that fractures induced by the hydraulic effect of the CTAB solution not only propagated along the horizontal bedding planes but also exhibited localized book-like fractures in the vertical direction. The phenomenon was observed at region VI in Fig. 8(g). This complex fracture pattern resulted in not only shale fragment-supported fractures (Fig. 8(k)) but also slip-supported fractures (Fig. 8(i)) within the core, significantly

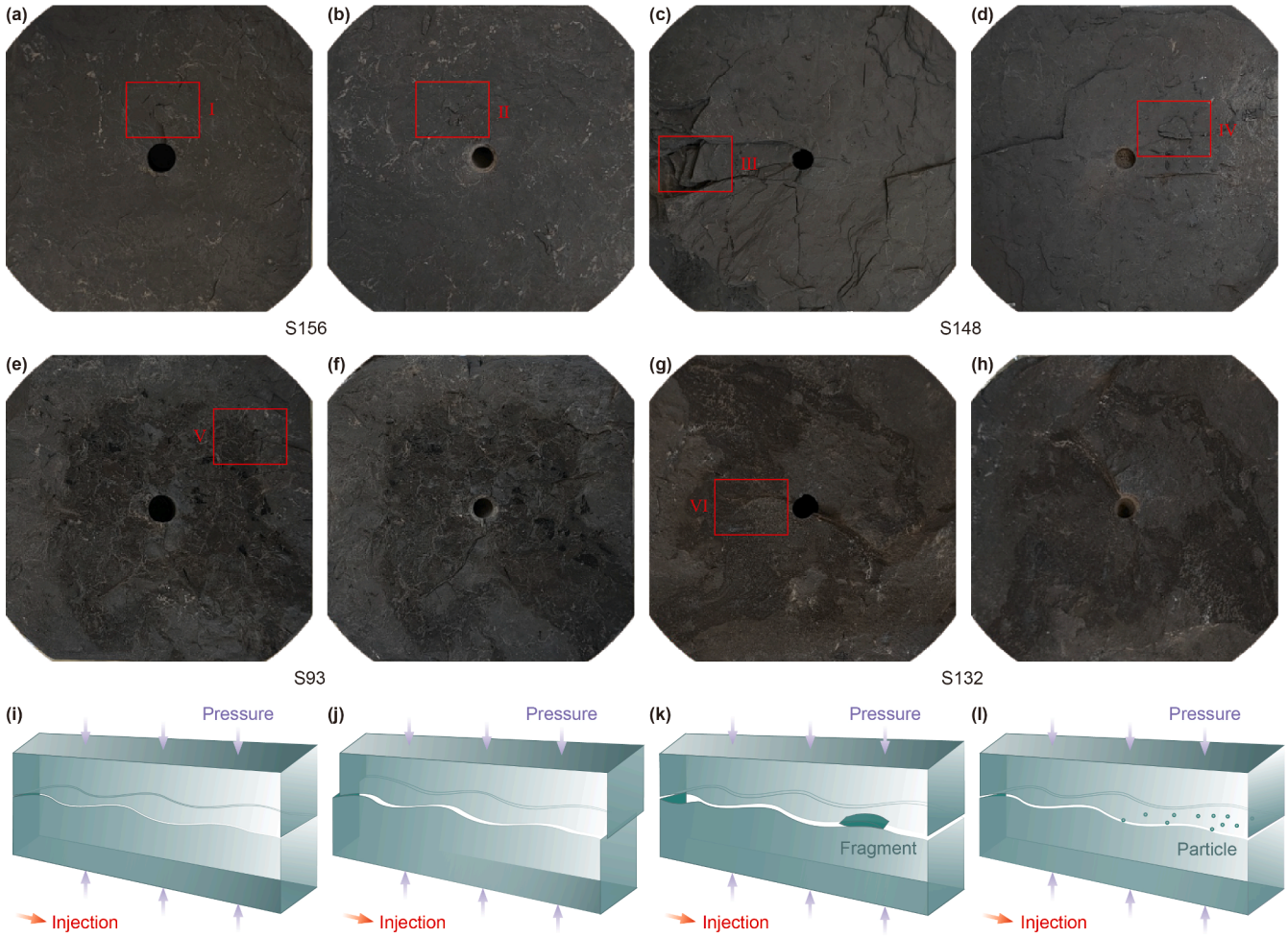

Fig. 8. Fracture surfaces and supporting patterns in full-diameter cores after injection of different fluids: (**a**) upper surface after KCl solution injection; (**b**) lower surface after KCl solution injection; (**c**) upper surface after CTAB solution injection; (**d**) lower surface after CTAB solution injection; (**e**) upper surface after SiO_2 solution injection; (**f**) lower surface after SiO_2 solution injection; (**g**) upper surface after CTAB and SiO_2 mixed solution injection; (**h**) lower surface after CTAB and SiO_2 mixed solution injection; (**i**) closed fracture; (**j**) sliding fracture; (**k**) fragment-supported fracture; (**l**) particle-supported fracture.

enhancing the anisotropic flow capacity of the fractures. Additionally, the areas of fragment detachment on the fracture surfaces formed potential preferential flow paths, thereby further enhancing the flow capacity. In contrast, the fracture surfaces induced by the CTAB and SiO_2 mixed solution appeared relatively flat and smooth, which resulted in better matching between the upper and lower fracture surfaces of the small particle-supported fracture. These flat and smooth fracture surfaces were prone to closure under confining pressure (Fig. 8(e)), significantly reducing the flow capacity. It is noteworthy that numerous small particles were observed on the fracture surfaces, further confirming that particle migration and accumulation cycles led to significant fluctuations in flow capacity during injections at different rates (Fig. 8(l)).

4.3. Simulation of percolation in hydraulically induced fractures

The velocity fields of localized fractures induced by different fluids in full-diameter shale cores are shown in Fig. 9. These fractures correspond to the localized hydraulically induced fractures shown in Fig. 7. It was found that the flow paths of localized fractures induced by KCl solution and CTAB solution gradually converged from a dendritic structure into a unified flow region, and their flow capacity increased progressively (Fig. 9(a–d)). This is due to the supporting effect of shale fragments around the unified flow region, while fractures at more distant locations tend to close in a scattered manner. The flow paths of localized fractures induced by the SiO_2 solution evolve from one dispersed dendritic structure to another. This behavior occurs because shale fragments provide structural support in the middle section of the fracture, while the fracture gradually closes in a scattered manner as the distance from these fragments increases. In localized fractures induced by the CTAB and SiO_2 mixed solution, only a narrow flow path was present in the middle and at the edge, severely restricting fluid flow in these fractures. It is observed at region VII in Fig. 9(d). The velocity in the narrower flow paths near the localized contact surface was significantly higher compared to that in the main flow paths. This phenomenon was observed at regions I (Fig. 9(a)), III (Fig. 9(b)), V and VI (Fig. 9(c)). As the flow path widens, the velocity decreases radially in localized areas, and the fluid gradually converges into the larger flow path (Fig. 9(f)). This phenomenon is mainly attributed to the lack of shale fragment support within these localized fracture zones. Notably, at the blind ends of the local fractures induced by the KCl solution, the SiO_2 solution, and the CTAB and SiO_2 mixed solution, there is virtually no fluid movement, and the fluid shows a stagnant state within these regions. This was observed at regions II (Fig. 9(a)) and VIII (Fig. 9(d)).

The pressure fields and flow streamline fields of localized fractures in full-diameter shale cores induced by different fluids

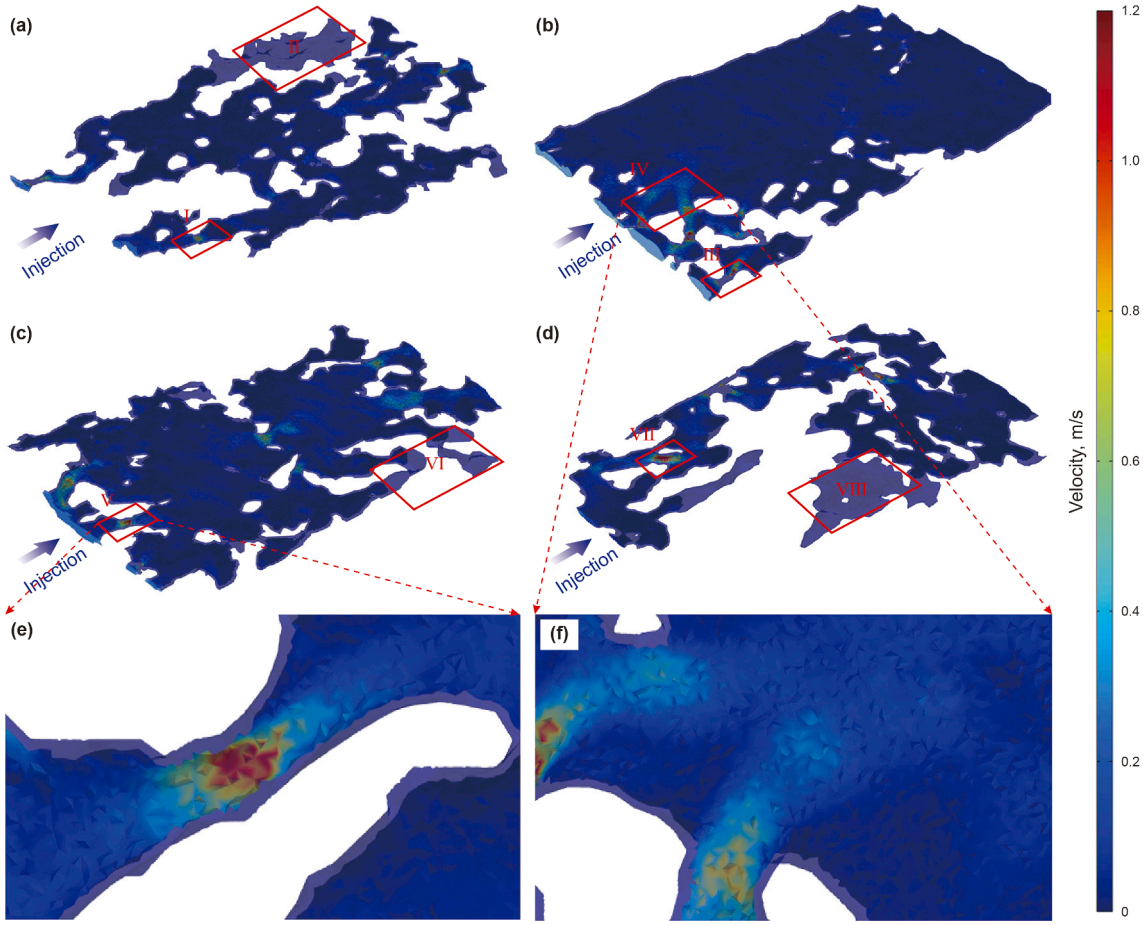

Fig. 9. Velocity fields in localized 3D fractures hydraulically induced by different fluids: (**a**) KCl solution; (**b**) CTAB solution; (**c**) SiO_2 solution; (**d**) CTAB and SiO_2 mixed solution; (**e**) enlarged view of V in (c); (**f**) enlarged view of VI in (b).

were obtained through numerical simulations (Fig. 10). The results demonstrate significant differences in pressure distribution and flow behavior among the different fluids within shale fractures. It was found that the localized fractures induced by the KCl solution exhibited higher injection pressure in the narrower flow paths in the upper-left region. The injected fluid converged toward the central area in a dendritic pattern and then dispersed again in branching flows, with a relatively gentle pressure gradient observed within the fracture network (Fig. 10(a)). This is attributed to the relatively uniform aperture of localized fractures supported by shale fragments, which facilitates smooth fluid flow. In contrast, the CTAB solution formed localized dendritic flow paths in the lower-right region of the fractures (Fig. 10(b)). Under identical injection rate conditions, the pressure gradient exhibited significant variations when the flow paths narrowed (Fig. 10(e)). This phenomenon results from strong fracture closure at this location, which constricted the flow pathways and consequently induced drastic changes in the pressure gradient. The SiO_2 solution exhibited the most gradual pressure gradient within localized fractures (Fig. 10(c)), indicating that shale fragments uniformly supported the fractures at this location, enabling fluid flow with a stable pressure gradient. This uniform self-supporting effect effectively prevents fracture closure, thereby maintaining high flow capacity. The CTAB and SiO_2 mixed solution form only a minor flow path at the edge of the central fracture zone (Fig. 10(f)), resulting in concentrated injection pressure at this location. It is observed at region II in Fig. 10(d). The injection pressure decreases rapidly after passing through this constriction, exhibiting a radial diffusion pattern. This phenomenon was observed at region II in Fig. 10(d). This indicates that the localized fractures at this location lack internal support from shale fragments, while the accumulation of fine particles within the preferential flow paths severely impedes fluid movement.

To quantitatively investigate the relationship between injection rate and pressure difference in fractures hydraulically induced by different fluids, the variation in pressure difference between the injection and outlet ends of localized fractures was analyzed under varying injection rates. It was found that within the localized fractures of each core, the pressure difference increased progressively with increasing injection rate, and the rate of increase also became more pronounced. At the same injection pressure, the fracture induced by the SiO_2 solution exhibited the highest flow capacity. The flow capacities of the localized fractures induced by the KCl solution and the CTAB solution were relatively similar. Notably, at low velocities ($u < 0.3$ m/s), the fracture induced by the KCl solution exhibited higher flow capacity. However, when the velocity exceeded 0.3 m/s, the flow capacity of the fractures induced by the CTAB solution gradually surpassed that of the fracture induced by the KCl solution.

The lowest flow capacity was observed in the localized fractures induced by the CTAB and SiO_2 mixed solution (Fig. 11(a)). Simulation results show that the flow capacity of localized fractures by each fluid follows the order: SiO_2 solution (S93) > CTAB solution (S148) and KCl solution (S156) > CTAB and SiO_2 mixed

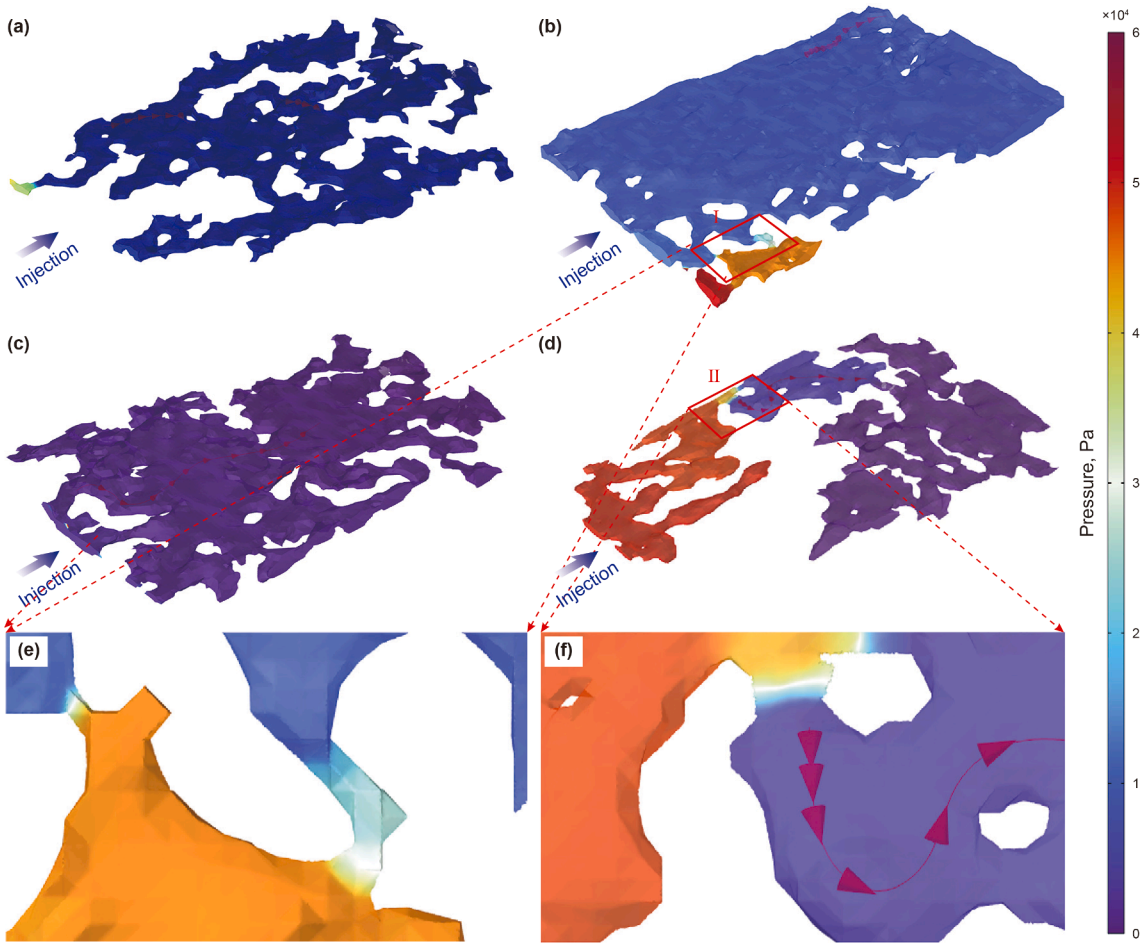

Fig. 10. Pressure and flow streamline fields in localized 3D fractures hydraulically induced by different fluids: (**a**) KCl solution; (**b**) CTAB solution; (**c**) SiO_2 solution; (**d**) CTAB and SiO_2 mixed solution; (**e**) enlarged of I in (b); (**f**) enlarged view of II in (d).

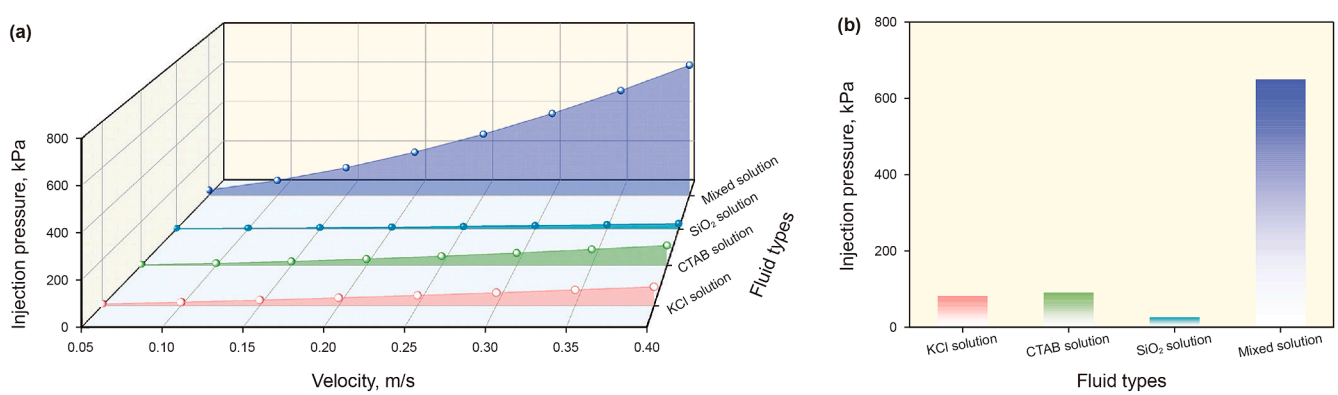

Fig. 11. (**a**) Injection pressure-velocity relationships for different fluids; (**b**) Injection pressure at 0.4 m/s.

solution (S132), which is consistent with the experimental results (Fig. 11(b)).

4.4. Discussion

The continental shale in the Songliao Basin is characterized by abundant layering (also known as bedding fracture), which represents the inherent micro-damage prior to shale hydration. For geotechnical structures with initial damage, the injection of fluids can induce new micro-damage at these pre-existing damaged sites. As micro-damage accumulates, it gradually evolves into macro-fractures, ultimately forming an effective fracture flow system. Additionally, the micro-structure of the shale bedding surfaces and sections also has a significant effect on the flow capacity of shale.

In continental shale reservoirs with extremely low permeability, pore sizes are typically at the nanoscale. Additionally, the shale of the Songliao Basin is typically an oil-wet reservoir (Sun

et al., 2021; Zhang et al., 2023a, 2023b), resulting in poor water imbibition capability of the shale matrix, which in turn inhibits the flow of the injected fluids within the shale matrix. Clay minerals are protected by CTAB and SiO_2 nanoparticles, reducing hydration effects and making fractured shale debris less prone to swelling and disintegration. This stabilization helps maintain a more consistent flow capacity. Moreover, fractures hydraulically induced by fluids gradually become essential paths for shale oil to flow from matrix pores to the wellbore.

5. Conclusions

In this study, the flow capacity of fractures hydraulically induced by different fluids in full-diameter shale cores from the Songliao Basin, China. The percolation behavior of the injected fluids in the hydraulically induced fractures was clarified. The main conclusions are summarized as follows:

(1) The injection of different fluids hydraulically induced fracture opening along the shale bedding planes, forming an effective flow system. The fracture surfaces were relatively flat and smooth, and no obvious fracture turning was observed.
(2) Shale fragments eroded and spalled near the injection end were transported to more distant locations and contributed to propping the fractures. The fracture openings at these locations increased, and the flow capacity was enhanced. This behavior differs from that observed in conventional hydraulic fracturing.
(3) Both the CTAB solution and the SiO_2 solution reduced shale surface hydration, which stabilized the mechanical properties at the fracture interfaces. As a result, shale fragments were less prone to swelling and disintegration, leading to a more stable flow capacity.
(4) The fracture flow capacities induced by the CTAB solution and the SiO_2 solution were both higher than that induced by the CTAB and SiO_2 mixed solution. The coupling effect of mixed solution severely inhibited shale hydration, making shale fragments less likely to detach, thereby preventing effective support of the fracture apertures.
(5) Hydraulic fractures induced by injection of the KCl solution, the SiO_2 solution, and the CTAB and SiO_2 mixed solution each formed only a single fracture along the preferential shale bedding plane. In contrast, the CTAB solution induced the formation of three distinct fractures at different horizontal levels along the shale bedding plane.
(6) As the spatial distance from the shale fragments increases, the fractures gradually exhibit dispersed closure. The velocity in the smaller flow paths near the closure is significantly higher than that in the main flow paths, resulting in a pronounced bypassing phenomenon. This hinders effective fluid percolation through the shale core.

CRediT authorship contribution statement

Hong-Tao Fu: Writing – original draft, Methodology, Investigation, Conceptualization. **Kao-Ping Song:** Writing – review & editing, Supervision, Resources, Funding acquisition. **Er-Long Yang:** Software, Resources, Investigation. **Yu Zhao:** Resources, Funding acquisition, Formal analysis. **Xi Xia:** Visualization, Supervision, Software, Conceptualization. **Li-Hao Liang:** Writing – review & editing, Methodology, Formal analysis.

Data availability statement

The data that support the findings of this study are available from the corresponding author upon reasonable request.

Declaration of competing interest

The authors declare no conflict of interest.

Acknowledgments

This work is supported by the Frontier and Fundamental Research of Active Nanofluids Flooding for Enhanced Oil Recovery through Discontinuous and Variable-circle Modes in High Temperature and High Salinity Offshore Oilfields (U22B6005); National Natural Science Foundation of China (No. 52274037); Study on Key Issues of Enhanced Oil Recovery of Gulong Shale Oil (DQYT-2022-JS-761).

Appendix A. Supplementary data

Supplementary data to this article can be found online at https://doi.org/10.1016/j.petsci.2025.09.035.

References

Avizo, 2019. Thermo Scientific Avizo Software User's Guide, Version 2019. Konrad-Zuse-Zentrum für informationstechnick, Berlin, Germany. https://assets.thermofisher.cn/TFS-Assets/MSD/Product-Guides/users-guide-avizo-software-2019.pdf.

Cui, F.L., Jin, X., Xia, J., Liu, H., Wu, H.A., Wang, F.C., 2023. Micromechanical mechanism of oil/brine/rock interfacial interactions based on first-principles calculations. J. Mol. Liq. 386, 122502. https://doi.org/10.1016/j.molliq.2023.122502.

Dou, L.R., Wen, Z.X., Wang, J.J., Wang, Z.M., He, Z.J., Liu, X.B., Zhang, N.N., 2022. Analysis of the world oil and gas exploration situation in 2021. Petrol. Explor. Dev. 49 (5), 1195–1209. https://doi.org/10.1016/S1876-3804(22)60343-4.

Fu, H.T., Song, K.P., Zhao, Y., Liang, L.H., Song, Q.J., Guo, H., 2024. Study on dynamic imbibition mechanism of matrix-fracture in three dimensions tight sandstone based on level set method. Phys. Fluids 36 (9), 092035. https://doi.org/10.1063/5.0215871.

Gao, Z.Y., Bai, L.X., Hu, Q.H., Yang, Z., Jiang, Z.X., Wang, Z.W., Xin, H.T., Zhang, L.L., Yang, A.D., Jia, L.D., Liu, Z.C., Ma, G.M., 2024. Shale oil migration across multiple scales: a review of characterization methods and different patterns. Earth Sci. Rev. 254, 104819. https://doi.org/10.1016/j.earscirev.2024.104819.

Guo, J.J., Di, K.X., Zhang, L.H., Zhao, Y.L., Tang, H.Y., Zhang, R.H., Tian, Y., 2024. Insights into in-situ imbibition behavior of fracturing fluid in propped shale fractures based on nuclear magnetic resonance: a case study from Longmaxi Formation shale, Sichuan Basin, China. Pet. Sci. 21 (1), 410–429. https://doi.org/10.1016/j.petsci.2023.09.023.

He, J.M., Li, X., Yin, C., Zhang, Y.X., Lin, C., 2020. Propagation and characterization of the micro cracks induced by hydraulic fracturing in shale. Energy 191, 116449. https://doi.org/10.1016/j.energy.2019.116449.

He, W.Y., Zhu, R.K., Cui, B.W., Zhang, S.C., Meng, Q., Bai, B., Feng, Z.H., Lei, Z.D., Wu, S.T., He, K., Liu, H., Sun, L.D., 2023. The geoscience frontier of Gulong shale oil: revealing the role of continental shale from oil generation to production. Engineering 28, 79–92. https://doi.org/10.1016/j.eng.2022.08.018.

Hong, X.Y., Jin, X., Shen, M., Fan, J.C., Wu, H.A., Wang, F.C., 2024. Enhancement of oil transport through nanopores via cation exchange in thin brine films at rock-oil interface. Adv. Geo-Energy Res. 12 (1), 22–34. https://doi.org/10.46690/ager.2024.04.03.

Hou, X.Y., Sheng, J.J., 2022. Experimental study on the imbibition mechanism of the Winsor type I surfactant system with ultra-low IFT in oil-wet shale oil reservoirs by NMR. J. Petrol. Sci. Eng. 216, 110785. https://doi.org/10.1016/j.petrol.2022.110785.

Hu, S.Y., Zhao, W.Z., Hou, L.H., Yang, Z., Zhu, R.K., Wu, S.T., Bai, B., Jin, X., 2020. Development potential and technical strategy of continental shale oil in China. Petrol. Explor. Dev. 47 (4), 877–887. https://doi.org/10.1016/S1876-3804(20)60103-3.

Karimi, M., Ghasemi, M., Babaei, M., Shahbazi, K., 2023. Molecular insight into inhibitory performance of CTAB surfactant for montmorillonite swelling; implications for drilling fluid design. Geoenergy Sci. Eng. 231, 221399. https://doi.org/10.1016/j.geoen.2023.212399.

Kim, S., Kim, K.H., Lim, J.T., 2023. Synergistic enhancement of productivity prediction using machine learning and integrated data from six shale basins of the

USA. Geoenergy Sci. Eng. 229, 212068. https://doi.org/10.1016/j.geoen.2023.212068.

Li, M., Wang, M., Zhao, C., Zhang, J.Y., Liu, Z., Zhao, X.B., Li, J.B., Chen, J.Y., 2024. Compositional differences of near-critical petroleum from closed pores to wellhead in Gulong shale oil play, Songliao Basin, NE China. Mar. Petrol. Geol. 167, 106968. https://doi.org/10.1016/j.marpetgeo.2024.106968.

Li, X.Y., Lei, X.L., Li, Q., 2023. Laboratory hydraulic fracturing in layered tight sandstones using acoustic emission monitoring. Geoenergy Sci. Eng. 223, 211510. https://doi.org/10.1016/j.geoen.2023.211510.

Liu, J.R., Sheng, J.J., Wang, X.K., Ge, H.K., Yao, E.D., 2019. Experimental study of wettability alteration and spontaneous imbibition in Chinese shale oil reservoirs using anionic and nonionic surfactants. J. Petrol. Sci. Eng. 175, 624–633. https://doi.org/10.1016/j.petrol.2019.01.003.

Lv, J.X., Hou, B., 2024. Fractures interaction and propagation mechanism of multi-cluster fracturing on laminated shale oil reservoir. Pet. Sci. 21 (4), 2600–2613. https://doi.org/10.1016/j.petsci.2024.02.007.

Ma, T.S., Yang, C.H., Chen, P., Wang, X.D., Guo, Y.T., 2016. On the damage constitutive model for hydrated shale using CT scanning technology. J. Nat. Gas Sci. Eng. 28, 204–214. https://doi.org/10.1016/j.jngse.2015.11.025.

Mcmahon, T.P., Larson, T.E., Zhang, T., Shuster, M., 2024. Geologic characteristics, exploration and production progress of shale oil and gas in the United States: an overview. Petrol. Explor. Dev. 51 (4), 925–948. https://doi.org/10.1016/S1876-3804(24)60516-1.

Meng, S.W., Tao, J.P., Li, T.J., Li, D.X., Wang, S.L., Yang, L., Liu, X., Liang, L.H., Liu, H., 2024. Mechanical characteristics and reservoir stimulation mechanisms of the Gulong shale oil reservoirs, the northern Songliao Basin. Pet. Sci. 21 (3), 2023–2036. https://doi.org/10.1016/j.petsci.2023.11.002.

Panton, R.L., 2013. Incompressible Flow. John Wiley and Sons Inc, Hoboken. https://doi.org/10.1002/9781118713075.

Shakya, S., Li, B.X., Etienne, X.L., 2022. Shale revolution, oil and gas prices, and drilling activities in the United States. Energy Econ. 108, 105877. https://doi.org/10.1016/j.eneco.2022.105877.

Shi, Z.P., Li, P.X., Liu, L.Y., 2023. Interactions between CTAB and montmorillonite by atomic force microscopy and molecular dynamics simulation. Colloids Surf. A Physicochem. Eng. Asp. 657, 130656. https://doi.org/10.1016/j.colsurfa.2022.130656.

Song, Y.L., Song, Z.J., Chen, Z.X., Mo, Y.S., Zhou, Q.C., Tian, S.Z., 2024. Simulation of CO_2 enhanced oil recovery and storage in shale oil reservoirs: unveiling the impacts of nano-confinement and oil composition. Adv. Geo-Energy Res. 13 (2), 106–118. https://doi.org/10.46690/ager.2024.08.05.

Sun, L.D., Cui, B.W., Zhu, R.K., Wang, R., Feng, Z.H., Li, B.H., Zhang, J.Y., Gao, B., Wang, Q.Z., Zeng, H.S., Liao, Y.H., Jiang, H., 2023. Shale oil enrichment evaluation and production law in Gulong Sag, Songliao Basin, NE China. Petroleum Exploration and Development 50 (3), 505–519. https://doi.org/10.1016/S1876-3804(23)60406-9.

Sun, L.D., Liu, H., He, W.Y., Li, G.X., Zhang, S.C., Zhu, R.K., Jin, X., Meng, S.W., Jiang, H., 2021. An analysis of major scientific problems and research paths of Gulong shale oil in Daqing Oilfield, NE China. Petroleum Exploration and Development 48 (3), 527–540. https://doi.org/10.1016/S1876-3804(21)60043-5.

US Energy Information Administration (EIA), 2013. Technically Recoverable Shale Oil and Shale Gas Resources. https://www.eia.gov/analysis/studies/worldshalegas/.

Wang, F.L., Feng, Z.H., Wang, X., Zeng, H.S., 2023a. Effect of organic matter, thermal maturity and clay minerals on pore formation and evolution in the Gulong Shale, Songliao Basin, China. Geoenergy Sci. Eng 223, 211507. https://doi.org/10.1016/j.geoen.2023.211507.

Wang, X., Wang, M., Li, J.B., Shao, H.M., Deng, Z.X., Wu, Y., 2022a. Thermal maturity: the controlling factor of wettability, pore structure, and oil content in the lacustrine Qingshankou shale, Songliao Basin. J. Petrol. Sci. Eng. 215, 110618. https://doi.org/10.1016/j.petrol.2022.110618.

Wang, X.J., Cui, B.W., Feng, Z.H., Shao, H.M., Huo, Q.L., Zhang, B., Gao, B., Zeng, H.S., 2023b. In-situ hydrocarbon formation and accumulation mechanisms of micro-and nano-scale pore-fracture in Gulong shale, Songliao Basin, NE China. Petrol. Explor. Dev. 50 (6), 1105–1115. https://doi.org/10.1016/S1876-3804(24)60465-9.

Wang, X.N., Li, J.R., Jiang, W.Q., Zhang, H., Feng, Y.L., Yang, Z., 2022b. Characteristics, current exploration practices, and prospects of continental shale oil in China. Adv. Geo-Energy Res. 6 (6), 454–459. https://doi.org/10.46690/ager.2022.06.02.

Xiao, F., Yang, J.G., Li, S.C., Yao, Y.L., Huang, Y.M., Gao, X.Y., 2024. Enrichment and movability of lacustrine tight shale oil for the first member of the Upper Cretaceous Qingshankou Formation in the Sanzhao Sag, Songliao Basin, NE China: Insights from saturated hydrocarbon molecules. Fuel 368, 131615. https://doi.org/10.1016/j.fuel.2024.131615.

Yang, K., Zhou, J.P., Xian, X.F., Zhou, L., Zhang, C.P., Tian, S.F., Lu, Z.H., Zhang, F.S., 2022. Chemical-mechanical coupling effects on the permeability of shale subjected to supercritical CO_2-water exposure. Energy 248, 123591. https://doi.org/10.1016/j.energy.2022.123591.

Yang, L., Sheng, X.C., Zhang, B., Yu, H.H., Wang, X.L., Wang, P., Mei, J., 2023. Propagation behavior of hydraulic fractures in shale under triaxial compression considering the influence of sandstone layers. Gas Sci. Eng. 110, 204895. https://doi.org/10.1016/j.jgsce.2023.204895.

Yang, Z., Zou, C.N., Wu, S.T., Lin, S.H., Pan, S.Q., Niu, X.B., Men, G.T., Tang, Z.X., Yotsuji, K., Tachi, Y., Sakuma, H., Kawamura, K., 2021. Effect of interlayer cations on montmorillonite swelling: comparison between molecular dynamic simulations and experiments. Appl. Clay Sci. 204, 106034. https://doi.org/10.1016/j.clay.2021.106034.

Yu, Z.Q., Ma, S.Z., Mallick, S., Wang, C., Zhao, H.B., Li, G., 2024. Prediction of shale oil "sweet spot" parameters centered on seismic prestack waveform inversion. Geoenergy Sci. Eng. 241, 213157. https://doi.org/10.1016/j.geoen.2024.213157.

Zhang, B., Guo, T.K., Chen, M., Wang, J.W., Cao, J.H., Wang, H.Y., Qu, Z.Q., 2024. Effect of bedding planes and property contrast between layers on the propagation mechanism of hydraulic fracture height in shale reservoirs. Comput. Geotech. 175, 106715. https://doi.org/10.1016/j.compgeo.2024.106715.

Zhang, C., Jia, S., Huang, X.H., Shi, X.T., Zhang, T., Zhang, L., Wang, F.T., 2024. Accurate characterization method of pores and various minerals in coal based on CT scanning. Fuel 358, 130128. https://doi.org/10.1016/j.fuel.2023.130128.

Zhang, J.Y., Zhu, R.K., Wu, S.T., Jiang, X.H., Liu, C., Cai, Y., Zhang, S.R., Zhang, T.S., 2023. Microscopic oil occurrence in high-maturity lacustrine shales: Qingshankou Formation, Gulong Sag, Songliao Basin. Pet. Sci. 20 (5), 2726–2746. https://doi.org/10.1016/j.petsci.2023.08.026.

Zhang, P.F., Lu, S.F., Li, J.Q., Chang, X.C., Zhang, J.J., Pang, Y.M., Lin, Z.Z., Chen, G., Yin, Y.J., Liu, Y.Q., 2023. Quantitative characterization of shale pore connectivity and controlling factors using spontaneous imbibition combined with nuclear magnetic resonance T_2 and T_1-T_2. Pet. Sci. 20 (4), 1947–1960. https://doi.org/10.1016/j.petsci.2023.03.011.

Zhang, S.F., Sheng, J.J., Shen, Z.Q., 2017. Effect of hydration on fractures and permeabilities in Mancos, Eagleford, Barnette and Marcellus shale cores under compressive stress conditions. J. Petrol. Sci. Eng. 156, 917–926. https://doi.org/10.1016/j.petrol.2017.06.043.

Zhao, W.Z., Guan, M., Liu, W., Bian, C.S., Li, Y.X., Wang, X.M., Xu, R.N., 2024. Low-to-medium maturity lacustrine shale oil resource and in-situ conversion process technology: recent advances and challenges. Adv. Geo-Energy Res. 12 (2), 81–88. https://doi.org/10.46690/ager.2024.05.01.

Zhao, W.Z., Bian, C.S., Li, Y.X., Zhang, J.Y., He, K., Liu, W., Zhang, B., Lei, Z.D., Liu, C., Zhang, J.Y., Guan, M., Liu, S.J., 2023. Enrichment factors of movable hydrocarbons in lacustrine shale oil and exploration potential of shale oil in Gulong Sag, Songliao Basin, NE China. Petroleum Exploration and Development 50 (3), 520–533. https://doi.org/10.1016/S1876-3804(23)60407-0.

Zhou, J., Wu, G.A., Geng, Y.N., Guo, Y.T., Chang, X., Peng, C.Y., Ai, C.Z., 2023. Laboratory study of the factors affecting hydraulic fracturing effect for inter-salt oil shale layers, Qianjiang Depression, China. Pet. Sci. 20 (3), 1690–1706. https://doi.org/10.1016/j.petsci.2023.01.002.

Zhuang, Y., Zhang, T.T., Liu, X.J., Zhang, S.F., Liang, L.X., Xiong, J., 2014. Intrinsic mechanisms of shale hydration-induced structural changes. J. Hydrol. 637, 131433. https://doi.org/10.1016/j.jhydrol.2024.131433.